

LA-UR- 09-00024

Approved for public release;
distribution is unlimited.

Title: Thermal expansion and decomposition of jarosite: A high-temperature neutron diffraction study

Author(s): H. Xu, Y. Zhao, S.C. Vogel, D.D. Hickmott, L.L. Daemen and M.A. Hartl

Intended for: Physics and Chemistry of Minerals



Los Alamos National Laboratory, an affirmative action/equal opportunity employer, is operated by the Los Alamos National Security, LLC for the National Nuclear Security Administration of the U.S. Department of Energy under contract DE-AC52-06NA25396. By acceptance of this article, the publisher recognizes that the U.S. Government retains a nonexclusive, royalty-free license to publish or reproduce the published form of this contribution, or to allow others to do so, for U.S. Government purposes. Los Alamos National Laboratory requests that the publisher identify this article as work performed under the auspices of the U.S. Department of Energy. Los Alamos National Laboratory strongly supports academic freedom and a researcher's right to publish; as an institution, however, the Laboratory does not endorse the viewpoint of a publication or guarantee its technical correctness.

**Thermal expansion and decomposition of jarosite:
A high-temperature neutron diffraction study**

Hongwu Xu,^{1,2*} Yusheng Zhao,² Sven C. Vogel,²

Donald D. Hickmott,¹ Luke L. Daemen,² and Monika A. Hartl²

¹Earth and Environmental Sciences Division

²Los Alamos Neutron Science Center

Los Alamos National Laboratory

Los Alamos, New Mexico 87545, USA

*Email: hxu@lanl.gov

Submitted to *Physics and Chemistry of Minerals*

December 2008

Abstract The structure of deuterated jarosite, $\text{KFe}_3(\text{SO}_4)_2(\text{OD})_6$, was investigated using time-of-flight neutron diffraction up to its dehydroxylation temperature. Rietveld analysis reveals that with increasing temperature, its c dimension expands at a rate ~ 10 times larger than that for a . This anisotropy of thermal expansion is due to rapid increase in the thickness of the (001) sheet of $[\text{Fe}(\text{O},\text{OH})_6]$ octahedra and $[\text{SO}_4]$ tetrahedra with increasing temperature. Fitting of the measured cell volumes yields a coefficient of thermal expansion, $\alpha = \alpha_0 + \alpha_1 T$, where $\alpha_0 = 1.01 \times 10^{-4} \text{ K}^{-1}$ and $\alpha_1 = -1.15 \times 10^{-7} \text{ K}^{-2}$. On heating, the hydrogen bonds, $\text{O1} \cdots \text{D}-\text{O3}$, through which the (001) octahedral-tetrahedral sheets are held together, become weakened, as reflected by increase in the $\text{D} \cdots \text{O1}$ distance and concomitant decrease in the $\text{O3}-\text{D}$ distance with increasing temperature. On further heating to 575 K, jarosite starts to decompose into nanocrystalline yavapaiite and hematite (as well as water vapor), a direct result of the breaking of the hydrogen bonds that hold the jarosite structure together.

Keywords Jarosite; Neutron diffraction; Thermal expansion; Decomposition; Hydrogen bonds; Crystal chemistry

Introduction

Jarosite, $\text{KFe}_3(\text{SO}_4)_2(\text{OH})_6$, and the related sulfates, which comprise the so-called “alunite supergroup” (Jambor 1999), commonly occur in acid drainage environments, as the weathering products of sulfide ore deposits. They are found in clays as modules and disseminations and in acid soils, where previously existing pyrite was oxidized into jarosite. They can also precipitate from aqueous sulfate due to oxidation of H_2S in epithermal environments and hot springs associated with volcanic activities (Papike et al. 2006). In 2004, jarosite was detected by the Mars Exploration Rover (MER) Mössbauer spectrometer (Klingelhöfer et al. 2004), which has been interpreted as strong evidence for the occurrence of large amounts of water (and possibly life) in the history of Mars. A recent study using laser desorption Fourier transform mass spectrometry revealed the presence of organic matters (such as glycine) in several jarosite samples (Kotler et al. 2008), thereby validating the hypothesis of possible existence of life on Mars.

In addition to its geological importance, jarosite is of considerable interest for its industrial applications (Dutrizac and Jambor 2000). Specifically, in the zinc industry, Zn is usually extracted from Zn-sulfides (such as sphalerite) by the so-called “roast-leach-electrolysis” process. However, these sulfides commonly contain Fe, typically 5 to 12 wt%, which needs to be removed. Precipitation of jarosite compounds has been found to be an effective means for the Fe removal, as they form quickly and are readily filterable and washable. This process operates at atmospheric pressure, rather than requiring an autoclave as for many hydrothermal processes, and is thus economical. Furthermore, the generated jarosite (in the form of mud) can be combined with other industrial wastes such as dump ferrous slag (DFS) and alkaline Al-surface cleaning waste (ASCW) as well as

small portions of Portland cement or lime to produce materials for construction applications (such as airfield runways and levee cores) (Mymrin et al. 2005). In addition, jarosite and its associated alunite-type phases have been proposed as potential hosts for the long-term immobilization of radioactive fission products and toxic heavy metals (Ballhorn et al. 1989; Kolitsch et al. 1999).

The structure of jarosite consists of $[\text{SO}_4]$ tetrahedra and distorted $[\text{Fe}(\text{O},\text{OH})_6]$ octahedra with K located in a 12-fold coordinated site (space group $R\bar{3}m$) (Fig. 1A) (Menchetti and Sabelli 1976; Stoffregen et al. 2000; Basciano and Peterson 2007). Each $[\text{Fe}(\text{O},\text{OH})_6]$ octahedron corner-shares four hydroxyl groups with neighboring $[\text{Fe}(\text{O},\text{OH})_6]$ octahedra and two oxygen atoms from two $[\text{SO}_4]$ tetrahedra (one above the Fe and one below), forming (001) sheets of $[\text{Fe}(\text{O},\text{OH})_6]$ and $[\text{SO}_4]$ perpendicular to the c axis. There are two types of crystallographically distinct $[\text{SO}_4]$ tetrahedra: one $[\text{SO}_4]$ pointing upward along c (c^+), and the other $[\text{SO}_4]$ pointing downward (c^-), which alternate zigzagly along the a -axes within the (001) layer (Fig. 1B). Each K is coordinated by 6 O atoms from $[\text{SO}_4]$ tetrahedra and 6 OH groups from $[\text{Fe}(\text{O},\text{OH})_6]$ octahedra. All 6 O atoms and all 6 OH groups are symmetrically identical, and thus the K site has a highly symmetrical coordination with 6 identical K-OH bonds and 6 identical K-O bonds (Papike et al. 2006).

The unique distribution of $[\text{Fe}(\text{O},\text{OH})_6]$ octahedra within the (001) layer coupled with the magnetic properties of Fe^{3+} makes jarosite a model compound for studying the spin frustration in two-dimensional *kagomé* lattices (composed of magnetic ions located at corners of triangles that are linked via corner-sharing) (Wills et al. 2000). Low-temperature neutron diffraction experiments reveal that jarosite exhibits long-range

magnetic ordering when cooled down below 65 K, as evidenced by the appearance of several magnetic reflections at $hkl/2, l = \text{odd}$ (Inami et al. 2000). The c-dimension of the magnetic unit cell is twice that of the conventional unit cell, and the magnetic structure belongs to the so-called “ $q = 0, 120^\circ$ type” with triangles of the spins having only positive chirality (Inami et al. 2000). The magnetic ordering is interpreted as a result of the coupling between the jarosite (001) layers exhibiting a net magnetization, which is mainly due to Dzyaloshinsky-Moriya (DM) anisotropic interactions (Grohol et al. 2003; Yildirim and Harris 2006).

Despite the detailed structural studies of jarosite at room and low temperatures, no information is available about its high-temperature structural behavior. The recent discovery of jarosite on Mars has spurred interests in its stability at various temperature, pressure and aqueous conditions (such as its pH). A number of thermochemical studies of jarosite and its analogues have been performed to determine their decomposition temperatures, enthalpies of formation, and enthalpies of dehydroxylation (Drouet and Navrotsky 2003; Drouet et al. 2004; Forray et al. 2005; Frost et al. 2005; Navrotsky et al. 2005). However, structural information for jarosite corresponding to its thermal behavior is still lacking. In particular, its coefficients and mechanisms of thermal expansion remain unknown. Since the high-temperature structural behavior of jarosite is likely to be related to changes in its hydroxyl behavior and since neutron scattering is sensitive to the position of hydrogen (and its isotopes), high-temperature neutron diffraction studies are particularly useful to unravel the mechanisms of its thermal expansion and decomposition.

In this study, we carried out *in situ* neutron diffraction of jarosite using a pulsed neutron source at temperatures up to 650 K (the sample started to decompose into yavapaiite $\text{KFe}(\text{SO}_4)_2$, hematite Fe_2O_3 and water vapor D_2O between 550 K and 575 K). To avoid the large incoherent scattering of neutrons by hydrogen, we synthesized deuterated jarosite, $\text{KFe}_3(\text{SO}_4)_2(\text{OD})_6$, using hydrothermal methods. Rietveld analysis of the time-of-flight neutron data allowed determination of structural parameters as a function of temperature. In particular, the atomic positions and atomic displacement parameters of jarosite at high temperatures have been obtained for the first time, and the structural effects on jarosite thermal expansion and stability are discussed.

Experimental methods

Sample synthesis

The jarosite sample used in this study was prepared via hydrothermal methods. First, 8.1 g of $\text{Fe}(\text{NO}_3)_3 \cdot 9\text{D}_2\text{O}$ (20 mmol) and 3.5 g of K_2SO_4 were dissolved separately in 25 mL D_2O . Second, the two solutions were mixed and stirred thoroughly in a 100 mL Teflon cup, which was then placed in a standard Parr autoclave. Third, the autoclave was sealed and heated at 433 K for 3 days. After cooling down to room temperature, the autoclave was opened, and the content filtered and washed with cold D_2O . Lastly, the resulted solid product was dried in air for one hour, placed in a vacuum oven at 383 K overnight and then stored in a desiccator. The product, a brown, well-crystallized powder, was confirmed to be single-phase jarosite by powder X-ray diffraction (Rigaku Ultima III, 40 keV, 50 mA, $\text{CuK}\alpha$ radiation). The K, Fe and S contents of the sample were measured by inductively coupled plasma atomic emission (ICP-AE) spectroscopy. The determined

weight concentrations are 7.66% K, 35.0% Fe and 12.6% S. These values are very close to the stoichiometric compositions of 7.81% K, 33.4% Fe and 12.8% S in $\text{KFe}_3(\text{SO}_4)_2(\text{OD})_6$, respectively. Thus in the following structural analysis, we treated the sample as having the ideal formula.

Neutron diffraction

Time-of-flight neutron diffraction experiments were performed at the High-Pressure Preferred Orientation (HiPPO) beamline of the Manuel Lujan, Jr. Neutron Scattering Center, Los Alamos National Laboratory. Sample powders were placed in a vanadium can 0.95 cm in diameter, and the can was mounted in an ILL-type high-temperature furnace with vanadium heating elements and heatshields for contamination-free diffraction data collection (Vogel et al. 2004). Data were collected under vacuum at room temperature and at temperatures from 350 to 650 K with an interval of 25 K. For each temperature point, three detector banks with nominal diffraction angles of 40° , 90° and 140° were simultaneously used. The heating rate was 5 K/min, and the dwell time at each targeted temperature (including an equilibration time of 5 min) was ~ 4 h.

Structure refinement

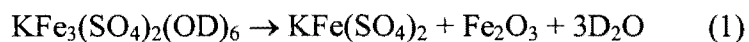
The neutron data were analyzed using the Rietveld method with the General Structure Analysis System (GSAS) program of Larson and Von Dreele (2000). The starting structural parameters for $\text{KFe}_3(\text{SO}_4)_2(\text{OD})_6$ at 298 K were taken from the neutron diffraction study of Menchetti and Sabelli (1976). We then used the refined structural parameters at 298 K as the starting parameters for the next highest temperature and

continued this procedure systematically with increasing temperature. For the runs at 575 K and 600 K, since a portion of the sample decomposed into yavapaiite, hematite and water vapor, we included yavapaiite and hematite as secondary phases in the Rietveld analyses. The starting structural parameters for yavapaiite and hematite were taken from the X-ray diffraction studies of Anthony et al. (1972) and Maslen et al. (1994), respectively. For the two highest temperature runs (625 and 650 K), only yavapaiite and hematite were present, and thus jarosite was excluded from the analyses. For each temperature point, two datasets from the detectors at $2\theta = 90^\circ$ and 140° were simultaneously analyzed (the 40° dataset was not used because of its relatively low resolution). The refinements proceeded as follows: after the scale factor and four background terms (Shifted Chebyshev function) for each histogram had converged, lattice parameters and phase fractions (for the runs at 575, 600, 625 and 650 K) were added and optimized. Fourteen or eighteen additional background terms were then added for each histogram, and the peak profiles were fitted to a TOF profile function (Von Dreele et al. 1982). On convergence of the preceding parameters, atomic coordinates and isotropic atomic displacement parameters for K, Fe, S, O, and D were refined, yielding R_{wp} values ranging from 1.33% to 1.43% and R_p from 0.87% to 0.98% (Table 1). The obtained unit-cell parameters, atomic coordinates, atomic displacement parameters, and selected bond parameters are listed in Tables 1-4, respectively. A representative pair of fitted patterns is plotted in Figure 2.

Results and discussion

Stability of jarosite

Our high-temperature neutron diffraction patterns indicate that the deuterated jarosite sample was stable up to 550 K. However, it started to decompose into yavapaiite, hematite and D₂O vapor when the temperature reached 575 K:



As shown in Figure 3, at 575 K, new diffraction peaks indicative of yavapaiite and hematite appeared, and the molar ratio, jarosite : yavapaiite: hematite, obtained from Rietveld analysis was 74.8:12.6:12.6. When the temperature was increased to 600 K, these new peaks grew, and more obviously, the original jarosite peaks (such as 003) became significantly weaker. The obtained molar ratio, jarosite : yavapaiite: hematite, at 600 K was 28.6:35.7:35.7. With further increasing temperature to 625 K, jarosite decomposed completely, as reflected by the disappearance of its diffraction peaks, and only yavapaiite and hematite were present. Thus the onset temperature of the jarosite dehydroxylation (T_d) lies between 550 and 575 K. This is generally consistent with previous thermal analyses of potassium jarosite, which show that the mass loss due to the dehydroxylation occurs in the temperature range 403-603 K (Frost et al. 2005). On the other hand, as in other hydroxyl-containing compounds such as portlandite (Xu et al. 2007), the measured dehydroxylation temperature can vary with sample purity, sample crystallinity and experimental conditions such as heating rate and water vapor pressure. These factors may account for some of the discrepancies in the reported T_d values for jarosite (Frost et al. 2005; Drouet and Navrotsky 2003).

Note that the overall intensities of the patterns at 600 and 625 K are much weaker than those at lower temperatures (Fig. 3). More specifically, diffraction peaks for the newly formed phases, yavapaiite and hematite, are broad and not well resolved. This

behavior suggests that these phases are probably nanocrystalline in nature, presumably due to the relatively low temperatures of their formation. Similar behavior has been observed in simple hydroxides such as brucite $[\text{Mg}(\text{OH})_2]$, where nanocrystalline MgO forms upon brucite dehydroxylation at 600 K (Sharma et al. 2004).

Thermal expansion

Although jarosite has a trigonal symmetry (space group $R\bar{3}m$), its structure is conventionally treated in terms of a hexagonal cell (defined by two unit-cell parameters a and c). On heating, both a and c increase, and thus cell volume V also increases (Fig. 4). However, as shown in Figures 4A and 4B (plotted on the same scale), the structural expansion of jarosite occurs at a much higher rate along the c -axis than along the a -axis and is thus highly anisotropic, which is consistent with the layered nature of its structure. To obtain the mean coefficients of thermal expansion (CTEs), we fitted the cell-parameter data to linear relations:

$$a = 7.2818 + 2.9756 \times 10^{-5}T \quad (2)$$

$$c = 16.9810 + 7.2339 \times 10^{-4}T \quad (3)$$

$$V = 779.727 + 3.9835 \times 10^{-2}T \quad (4)$$

The derived mean CTEs of $\text{KFe}_3(\text{SO}_4)(\text{OD})_6$ in the temperature range 298-575 K are: $\alpha_a = 4.0814 \times 10^{-6} \text{ K}^{-1}$; $\alpha_c = 4.2066 \times 10^{-5} \text{ K}^{-1}$; and $\alpha_V = 5.0322 \times 10^{-5} \text{ K}^{-1}$. Thus the c -axis expands ~10 times more rapidly than the a -axis with increasing temperature.

The cell volume data can also be fitted to a more general equation for thermal expansion:

$$V(T) = V_0 \exp[\int \alpha(T) dT] \quad (5)$$

where V_0 is the volume at a chosen reference temperature, T_0 , and $\alpha(T)$ is the thermal expansion coefficient, having the form:

$$\alpha(T) = \alpha_0 + \alpha_1 T \quad (6)$$

Using $T_0 = 298$ K, the fit yielded the following parameters: $V_0 = 790.99 \text{ \AA}^3$, $\alpha_0 = 1.01 \times 10^{-4} \text{ K}^{-1}$, and $\alpha_1 = -1.15 \times 10^{-7} \text{ K}^{-2}$. This fit is excellent, as indicated by an R^2 value of 0.995 and that the refined V_0 is approximately the same as the measured V_0 (791.28 \AA^3).

To the best of our knowledge, the obtained CTEs represent the first measurement of thermal expansion for jarosite and its related alunite group. The α_V value of $5.0322 \times 10^{-5} \text{ K}^{-1}$ falls within the α_V range for common compounds. However, it is significantly smaller than the α_V values of many other hydroxyl-bearing minerals with a layered structure. For example, brucite, $\text{Mg}(\text{OH})_2$, has an α_V of $10.9 \times 10^{-5} \text{ K}^{-1}$ (Redfern and Wood 1992), about two times that of jarosite. On the other hand, like brucite, jarosite exhibits large anisotropy in axial thermal expansion with a much higher CTE along the c axis (normal to the layer) than perpendicular to c . As detailed below, the thermal behavior of jarosite is due to the corresponding changes in its bonding parameters with increasing temperature.

Structural variation

Figure 5 shows variation of isotropic displacement factors (U_{iso}) of K, Fe, S, O and D with temperature. As expected, for a given element, its U_{iso} increases with increasing temperature. At a given temperature, $U_{iso}(\text{Fe}) < U_{iso}(\text{S}) \approx U_{iso}(\text{O}) < U_{iso}(\text{D}) \approx U_{iso}(\text{K})$. These trends are consistent with the decreased bond strengths from Fe to S/O to D/K (with their neighboring atoms), as $U (= kT/f)$, where k is the Boltzman constant, T absolute

temperature, and f the bond force constant) is inversely proportional to the bond force constant. Generally, the lighter the element, the weaker the bond strength and thus the larger the U_{iso} . However, exceptions do occur, depending on the bonding configuration of a given atom in the structure. In jarosite, K is situated between the (001) $[\text{Fe}(\text{O},\text{OH})_6]/[\text{SO}_4]$ sheets (Fig. 1A) and thus has relatively weaker electrostatic interactions with its adjacent O and OD. As a result, K has similarly high U_{iso} values to D, although it is much heavier.

As describe above, the jarosite structure is based on (001) sheets of $[\text{Fe}(\text{O},\text{OH})_6]$ octahedra and $[\text{SO}_4]$ tetrahedra (Fig. 1A). $[\text{Fe}(\text{O},\text{OH})_6]$ octahedra are linked via corner-sharing, forming six- and three-membered rings perpendicular to the c-axis (Fig. 1B). Each three-membered $[\text{Fe}(\text{O},\text{OH})_6]$ ring is connected to one $[\text{SO}_4]$ tetrahedron through one of the two sets of apical vertices, and neighboring $[\text{SO}_4]$ tetrahedra point to opposite directions (c+ or c-). Therefore, among the four O atoms in a $[\text{SO}_4]$ tetrahedron, three of them (O2) are each shared by one S and one Fe, but the fourth O (O1) is bonded only to one S (Fig. 1C). Since O1 is underbonded relative to O2, the S-O1 distance is expected to be shorter than S-O2; structure refinement of jarosite at room temperature shows that its S-O1 and S-O2 distances are 1.437 and 1.479 Å, respectively. These values fall within the observed S-O distances for 112 refined sulfate structures, which vary from 1.394 to 1.578 Å (Hawthorne et al. 2000). However, the S-O2 value of 1.479 Å is very close to the grand mean S-O distance, 1.473 Å, calculated from the 112 sulfate structures, whereas S-O1 is significantly lower. This observation can be explained using a formal charge model that was initially developed to explain local structures in alkaline-earth boroaluminates (Bunker et al. 1991). In this model, only network-forming cations are considered. The

charge donated by different cations is taken to be the cation charge divided by the cation coordination number, as in Pauling's second rule (Pauling 1960) and Brown and Shannon's treatment of bond strengths (Brown and Shannon 1973). In the case of jarosite; each S^{6+} cation donates a charge of $+6/4$ (or $+1.5$), and each Fe^{3+} donates a charge of $+3/6$ (or $+0.5$). Because O2 is bonded to one S^{6+} and one Fe^{3+} , it has a net charge of zero, resulting in a typical S-O distance associated with O2. On the other hand, as O1 is bonded only to one S^{6+} , it receives a charge of $+1.5$ and has a net charge of -0.5 . To compensate for this charge deficiency, S-O1 bond needs to be strengthened, thereby causing the contraction of S-O1.

With increasing temperature, S-O1 increases from 1.437 Å at 298 K to 1.474 Å at 575 K (Table 4). This behavior is consistent with the larger thermal expansion of the c-dimension, as S-O1 is parallel to the c-axis (Fig. 1C). On the other hand, S-O2 decreases from 1.479 Å at 298 K to 1.458 Å at 575 K. This S-O2 shortening can be explained in terms of $[Fe(O,OH)_6]$ octahedral tilting. On heating, the Fe-O3-Fe angle becomes smaller (from 133.77° at 298 K to 133.51° at 575 K, Table 4). Since each $[SO_4]$ tetrahedron shares three O2 atoms with a three-membered $[Fe(O,OH)_6]$ ring (one O2 from each $[Fe(O,OH)_6]$ octahedron) (Fig. 1B), the narrowing of Fe-O3-Fe effectively decreases the O2-O2 distance of the $[SO_4]$ tetrahedron, which causes shortening of the S-O2 bond. Moreover, as shown in Fig. 1A, $[Fe(O,OH)_6]$ octahedral layers are puckered, rather than being flat planar (which would correspond to a Fe-O3-Fe angle of 180°). Thus the decrease in the Fe-O3-Fe angle results in an increase in the degree of the (001) layer puckering via octahedral tilting. As a result, the overall structure expands along the c-axis but contracts parallel to the (001) plane. On the other hand, individual $[Fe(O,OH)_6]$

octahedra expand with increasing temperature, as reflected by the larger Fe-O2 and Fe-O3 distances. This causes expansion of the structure along both a- and c-axis. It appears that the net increase in a resulting from the thermal expansion of $[\text{Fe}(\text{O},\text{OH})_6]$ octahedra is largely canceled by the decrease due to the octahedral layer puckering, and thus a only shows a slight expansion. By contrast, both octahedral expansion and tilting contribute to the structural expansion along the c-axis, which, together with the S-O1 lengthening, leads to a much larger expansion along c .

Although jarosite exhibits a larger thermal expansion along the c axis (normal to the layer) than along a , as observed in other hydrous minerals with a layered structure, its volume expansion coefficient (α_V) is significantly smaller. In other words, the overall jarosite structure is less flexible in terms of expansion at elevated temperatures. This behavior can be interpreted on the basis of its unique structural characteristics. For many layered hydrous minerals (such as brucite $[\text{Mg}(\text{OH})_2]$), their structures can be treated as consisting of a structural layer (e.g., the $[\text{MgO}_6]$ layer in brucite) and the interlayer in which weak bonds (e.g., van der Waals forces) are operating. Thus the thermal expansion of these layered structures is due to that of both the structural layer and interlayer, where the latter typically plays a more significant role. In contrast, the jarosite structure is comprised only of layers of $[\text{Fe}(\text{O},\text{OH})_6]$ octahedra and $[\text{SO}_4]$ tetrahedra (Fig. 1A), lacking a distinct interlayer as in other hydrous structures. The absence of the interlayer is due to the constraint that neighboring $[\text{SO}_4]$ tetrahedra linked to different $[\text{Fe}(\text{O},\text{OH})_6]$ octahedra layers must have the same height along the c-axis (Fig. 1A); there is only one crystallographically distinct S in the unit cell of jarosite. Hence, the thermal expansion of

jarosite is determined solely by the flexibility of its $[\text{Fe}(\text{O},\text{OH})_6]/[\text{SO}_4]$ sheets, resulting in a smaller α_V compared with those of other layered hydrous compounds.

Despite the absence of a distinct weak-bonding interlayer in jarosite, the sheets of $[\text{Fe}(\text{O},\text{OH})_6]$ and $[\text{SO}_4]$ polyhedra are held together by the interstitial K^+ cation via the K-O2 and K-O3 bonds and the hydrogen bonding between O1 and D, $\text{O1}\cdots\text{D}-\text{O3}$ (Fig. 1C). As in other layered hydrous structures, these bonds are weaker than the bonds within the octahedral/tetrahedral sheets. As a result, the K-O2, K-O3 and $\text{D}\cdots\text{O1}$ distances exhibit relatively larger increases with increasing temperature (Table 4). In particular, the $\text{D}\cdots\text{O1}$ attraction, which operates between a given D (or H) and its closest O1 from the $[\text{SO}_4]$ tetrahedron of the neighboring $[\text{Fe}(\text{O},\text{OH})_6]/[\text{SO}_4]$ sheet (Fig. 1C), becomes weakened, as manifested by the increase in $\text{D}\cdots\text{O1}$ distance (Fig. 6A). In contrast, the O3-D bond length shows decreases on heating (Fig. 6B), suggesting that the O3-D bond becomes somewhat stronger. In other words, in the $\text{O1}\cdots\text{D}-\text{O3}$ bonding configuration, with increasing temperature, the O3 atoms pull the D closer, thereby effectively weakening the $\text{D}\cdots\text{O1}$ attraction. Hence, the interatomic interactions of D with its neighboring O atoms are interdependent and are largely driven by the thermal motion of D at elevated temperatures.

Mechanism of jarosite decomposition

It is conceivable that the stability of jarosite is dictated by the stability of the hydrogen bond, $\text{O1}\cdots\text{D}-\text{O3}$, as it, along with K^+ , holds the structural sheets of $[\text{Fe}(\text{O},\text{OH})_6]$ octahedra and $[\text{SO}_4]$ tetrahedra together. Once this hydrogen bond is broken due to high-temperature dehydroxylation, the jarosite structure disintegrates into yavapaiite, hematite

and water vapor. More specifically, $[\text{Fe}(\text{O},\text{OH})_6]$ octahedra become $[\text{FeO}_6]$ octahedra after dehydroxylation, and one third of the $[\text{FeO}_6]$ octahedra combine with $[\text{SO}_4]$ tetrahedra, via corner-sharing, forming $[\text{Fe}(\text{SO}_4)_2]$ sheets parallel to the (001) plane. These sheets are linked together by interstitial 10-coordinated K^+ , resulting in a layered compound, yavapaiite. In the mean time, the remaining two thirds of the $[\text{FeO}_6]$ octahedra are connected via edge-sharing to form gibbsite-type octahedral layers, and the latter are stacked, via face-sharing, along the c-axis, forming hematite. Given the structural relations among jarosite, yavapaiite and hematite, there may be certain topotactic relations between the decomposed jarosite and newly formed yavapaiite and hematite. Specifically, the layered nature of all the three phases may result in the following relation: $(001)_{\text{jarosite}} // (001)_{\text{yavapaiite}} // (001)_{\text{hematite}}$ OR $c_{\text{jarosite}} // c_{\text{yavapaiite}} // c_{\text{hematite}}$. This type of topotactic reaction (i.e., structurally controlled) mechanism has been found responsible for the thermal decomposition of many minerals including hydroxides, oxyhydroxides and carbonates (Sharma et al. 2004; Floquet and Niepce 1978). The occurrence of topotactic relations among jarosite, yavapaiite and hematite, however, would require verification by other techniques such as high-resolution transmission electron microscopy.

Conclusions

We have studied the stability and structural behavior of deuterated jarosite in the temperature range 298-650 K using neutron diffraction in conjunction with Rietveld analysis. Our results show that jarosite is stable up to 550 K, above which it starts to decompose into nanocrystalline yavapaiite and hematite. With increasing temperature,

both the a and c dimension of jarosite expand, but the latter expands at a rate ~ 10 times larger, as is consistent with the layered nature of its structure. On the other hand, because of the lack of a distinct weak-bonding interlayer between adjacent (001) sheets of $\text{Fe}(\text{O},\text{OH})_6$ octahedra and $[\text{SO}_4]$ tetrahedra, the volume expansion coefficient of jarosite is significantly smaller than those of many other hydroxyl-bearing minerals with a layered structure. At a given temperature, the amplitudes of thermal vibration of D and K are much larger than those for Fe, O and S, implying their weaker bonding with surrounding atoms. Correspondingly, on heating, the $\text{D}\cdots\text{O1}$ distance of the hydrogen bond $\text{O1}\cdots\text{D}-\text{O3}$ increases, which suggests weakened hydrogen bonding between neighboring (001) tetrahedral/octahedral sheets. By contrast, the $\text{O3}-\text{D}$ bond becomes stronger with increasing temperature, a trend also observed in simple hydroxides such as portlandite.

Acknowledgments We thank M.S. Rearick for carrying out compositional analysis of the jarosite sample. This work has benefited from the use of the Lujan Neutron Scattering Center at LANSCE, which is funded by the Department of Energy's Office of Basic Energy Sciences. Los Alamos National Laboratory is operated by Los Alamos National Security, LLC, under DOE Contract DE-AC52-06NA25396.

References

- Anthony JW, McLean WJ, Laughon RB (1972) The crystal structure of yavapaiite: a discussion. *American Mineralogist* 57: 1546-1549.
- Ballhorn R, Brunner H, Schwab RG (1989) Artificial compounds of the crandallite type: a new material for separation and immobilization of fission products. *Sci Basis Nucl Waste Manag* 12: 249-252.
- Basciano LC, Peterson RC (2007) Jarosite-hydronium jarosite solid-solution series with full iron site occupancy: Mineralogy and crystal chemistry. *American Mineralogist* 92: 1464-1473.
- Brown ID, Shannon RD (1973) Empirical bond-strength-bond-length curves for oxides. *Acta Crystallogr A* 29: 266-282.
- Bunker BC, Kirkpatrick RJ, Brow RK (1991) Local structure of alkaline-earth boroaluminate crystals and glasses: I. Crystal chemical concepts – structural predictions and comparisons to known crystal structures. *J Am Ceram Soc* 74: 1425-1429.
- Drouet C, Navrotsky A (2003) Synthesis, characterization and thermochemistry of K-Na-H₃O jarosites. *Geochimica et Cosmochimica* 67: 2063-2076.
- Drouet C, Pass KL, Baron D, Draucker S, Navrotsky A (2004) Thermochemistry of jarosite-alunite and natrojarosite-natroalunite solid solutions. *Geochimica et Cosmochimica* 68: 2197-2205.
- Dutrizac JE, Jambor JL (2000) Jarosite and their application in hydrometallurgy. In C.N. Alpers, J.L. Jambor, Eds., *Sulfate Minerals: Crystallography, Geochemistry, and Environmental Significance, Reviews in Mineralogy and Geochemistry, Vol. 40*, Mineralogical Society of America, Washington DC, 405-452.

Floquet N, Niepce JC (1978) Three-fold transformation twin in the topotactic decomposition of cadmium carbonate crystals. *Journal of Materials Science* 13: 766-776.

Forray FL, Drouett C, Navrotsky A (2005) Thermochemistry of yavapaiite $KFe(SO_4)_2$: formation and decomposition. *Geochimica et Cosmochimica* 69: 2133-2140.

Frost RL, Weier ML, Martens W (2005) Thermal decomposition of jarosites of potassium, sodium and lead. *Journal of Thermal Analysis and Calorimetry*, 82, 115-118.

Grohol D, Nocera DG, Papoutsakis D (2003) Magnetism of pure iron jarosites. *Physical Review B* 6706: 4401-4401.

Hawthorne FC, Krivovichev SV, Burns PC (2000) The crystal chemistry of sulfate minerals. In C.N. Alpers, J.L. Jambor, Eds., *Sulfate Minerals: Crystallography, Geochemistry, and Environmental Significance*, *Reviews in Mineralogy and Geochemistry*, Vol. 40, Mineralogical Society of America, Washington DC, 1-112.

Inami T, Nishiyama M, Meegawa S, Oka Y (2000) Magnetic structure of the *kagomé* lattice antiferromagnet potassium jarosite $KFe_3(OH)_6(SO_4)_2$. *Physical Review B*, 61, 12181-12186.

Jambor JL (1999) Nomenclature of the alunite supergroup. *Canadian Mineralogist*, 37, 1323-1341.

Klingelhöfer G, Morris RV et al. (2004) Jarosite and hematite at Meridiani Planum from Opportunity's Mössbauer spectrometer. *Science* 306: 1740-1745.

Kolitsch U, Tiekink ERT, Slade PG, Taylor MR, Pring A (1999) Hinsdalite and plumbogummite, their atomic arrangements and disordered lead sites. *Eur J Mineral* 11: 513-520.

- Kotler JM, Hinman NW, Yan B, Stoner DL, Scott JR (2008) Glycine identification in natural jarosites using laser desorption Fourier transform mass spectrometry: Implications for the search for life on mars. *Astrobiology* 8: 253-266.
- Larson AC, Von Dreele RB (2000) GSAS—general structure analysis system. Los Alamos National Laboratory Report No. LAUR 86–748. Los Alamos National Laboratory, Los Alamos.
- Maslen EN, Strel'tsov VA, Strel'tsova NR, Ishizawa N (1994) Synchrotron X-ray study of the electron density in alpha Fe_2O_3 . *Acta Crystallographica B*50: 435-441.
- Menchetti S, Sabelli C (1976) Crystal chemistry of the alunite series: crystal structure refinement of alunite and synthetic jarosite. *N Jahrb Miner Monatsh H* 9: 406-417.
- Mymrin VA, Ponte HA, Impinnisi PR (2005) Potential application of acid jarosite wastes as the main component of construction materials. *Construction and Building Materials* 19: 141-146.
- Navrotsky A, Forray FL, Drouet C (2005) Jarosite stability on Mars. *Icarus* 176: 250-253.
- Papike JJ, Karner JM, Shearer CK (2006) Comparative planetary mineralogy: Implications of martian and terrestrial jarosite. A crystal chemical perspective. *Geochimica et Cosmochimica Acta* 70: 1309-1321.
- Pauling L (1960) *The Nature of Chemical Bond*, 3rd Ed. Cornell University Press, Ithaca, NY.
- Redfern SAT, Wood BJ (1992) Thermal expansion of brucite, $\text{Mg}(\text{OH})_2$. *American Mineralogist* 77: 1129-1132.

Sharma R, Mckelvy MJ, Bearat H, Chizmeshya AVG, Carpenter RW (2004) In-situ nanoscale observations of the $\text{Mg}(\text{OH})_2$ dehydroxylation and rehydroxylation mechanisms. *Philosophical magazine* 84: 2711-2729.

Stoffregen RE, Alpers CN, Jambor JL (2000) Alunite-jarosite crystallography, thermodynamics, and geochronology. In C.N. Alpers, J.L. Jambor, Eds., *Sulfate Minerals: Crystallography, Geochemistry, and Environmental Significance, Reviews in Mineralogy and Geochemistry*, Vol. 40, Mineralogical Society of America, Washington DC, 453-479.

Vogel SC, Hartig C, Lutterotti L, Von Dreele RB, Wenk HR Williams DJ (2004) Texture measurements using the new neutron diffractometer HIPPO and their analysis using the Rietveld method. *Powder Diffraction* 19: 65-68.

Von Dreele RB, Jorgensen JD, Windsor CG (1982) Rietveld refinement with spallation neutron powder diffraction data. *J Applied Cryst* 15:581–589

Wills AS, Harrison A, Ritter C, Smith RI (2000) Magnetic properties of pure and diamagnetically doped jarosites: Model *kagome'* antiferromagnets with variable coverage of the magnetic lattice. *Physical Review B* 61: 6156-6169.

Xu H, Zhao Y, Vogel SC, Daemen LL, Hickmott DD (2007) Anisotropic thermal expansion and hydrogen bonding behavior of portlandite: A high-temperature neutron diffraction study. *Journal of Solid State Chemistry* 180: 1519-1525.

Yildirim T, Harris AB (2006) Magnetic structure and spin waves in the Kagome jarosite compound $\text{KFe}_3(\text{SO}_4)_2(\text{OH})_6$. *Physical Review B* 73: 214446.

Table 1 Unit-cell parameters of deuterated jarosite and agreement indices of the refinements

T (K)	a (Å)	c (Å)	V (Å ³)	R_{wp} (%)	R_p (%)
298	7.29013(6)	17.1921(2)	791.28(1)	1.33	0.87
350	7.29109(6)	17.2293(2)	793.20(1)	1.33	0.87
375	7.29275(6)	17.2514(2)	794.58(1)	1.33	0.87
400	7.29422(6)	17.2713(2)	795.82(1)	1.33	0.88
425	7.29541(7)	17.2916(2)	797.02(1)	1.33	0.89
450	7.29603(7)	17.3129(3)	798.13(1)	1.35	0.92
475	7.29644(7)	17.3316(3)	799.08(1)	1.35	0.93
500	7.29702(7)	17.3478(3)	799.96(1)	1.42	0.97
525	7.29759(7)	17.3632(3)	800.79(2)	1.43	0.98
550	7.29760(8)	17.3761(3)	801.39(2)	1.42	0.96
575	7.29775(10)	17.3854(4)	801.85(2)	1.42	0.89

Table 2 Atomic coordinates of deuterated jarosite^a

T(K)	z(S)	z(O1)	x(O2)	z(O2)	x(O3)	z(O3)	x(D)	z(D)
298	0.3077(2)	0.3913(1)	0.22320(7)	-0.05488(5)	0.12731(7)	0.13499(6)	0.19585(8)	0.10988(5)
350	0.3070(2)	0.3907(1)	0.22323(7)	-0.05518(5)	0.12741(7)	0.13500(6)	0.19555(8)	0.10978(5)
375	0.3066(2)	0.3904(1)	0.22338(7)	-0.05532(5)	0.12746(7)	0.13504(6)	0.19533(8)	0.10971(5)
400	0.3061(2)	0.3901(1)	0.22339(7)	-0.05547(5)	0.12751(8)	0.13497(6)	0.19523(8)	0.10966(5)
425	0.3057(2)	0.3898(1)	0.22346(7)	-0.05562(5)	0.12754(8)	0.13497(7)	0.19506(8)	0.10957(6)
450	0.3053(2)	0.3895(1)	0.22347(7)	-0.05573(6)	0.12755(8)	0.13502(7)	0.19490(8)	0.10959(6)
475	0.3051(2)	0.3893(1)	0.22347(7)	-0.05581(6)	0.12761(8)	0.13502(7)	0.19480(9)	0.10961(6)
500	0.3045(2)	0.3889(1)	0.22349(7)	-0.05581(6)	0.12765(9)	0.13491(7)	0.19467(9)	0.10967(6)
525	0.3041(3)	0.3887(1)	0.22348(8)	-0.05578(6)	0.12761(9)	0.13492(8)	0.19449(9)	0.10979(6)
550	0.3038(3)	0.3885(1)	0.22355(9)	-0.05562(7)	0.1276(1)	0.13487(9)	0.1942(1)	0.11000(7)
575	0.3035(4)	0.3883(2)	0.2236(1)	-0.05566(9)	0.1276(1)	0.1349(1)	0.1941(2)	0.10994(9)

^a $x(K) = y(K) = z(K) = 0$; $x(S) = y(S) = 0$; $x(Fe) = -y(Fe) = -z(Fe) = 1/6$; $x(O1) = y(O1) = 0$; $x(O2) = -y(O2)$; $x(O3) = -y(O3)$; $x(D) = -y(D)$.

Table 3 Isotropic atomic displacement parameters of deuterated jarosite^a

T(K)	$U_{iso}(\text{K})$	$U_{iso}(\text{S})$	$U_{iso}(\text{Fe})$	$U_{iso}(\text{O})^b$	$U_{iso}(\text{D})$
298	2.9(1)	1.10(7)	0.83(2)	1.21(1)	2.72(3)
350	3.0(1)	1.19(7)	0.89(2)	1.29(1)	2.89(3)
375	3.2(1)	1.27(7)	0.94(2)	1.38(1)	3.08(3)
400	3.4(1)	1.40(7)	1.00(2)	1.46(1)	3.22(3)
425	3.5(1)	1.46(7)	1.05(2)	1.53(2)	3.38(3)
450	3.7(1)	1.54(7)	1.09(2)	1.59(2)	3.50(4)
475	3.8(1)	1.54(8)	1.12(2)	1.64(2)	3.59(4)
500	3.9(1)	1.63(8)	1.18(2)	1.67(2)	3.57(4)
525	3.8(1)	1.70(8)	1.21(2)	1.74(2)	3.60(4)
550	3.8(1)	1.77(9)	1.26(2)	1.78(2)	3.62(4)
575	3.9(2)	1.76(11)	1.34(3)	1.86(3)	3.60(6)

^aThe unit of U_{iso} : $\text{\AA}^2/100$; ^bThe U_{iso} 's for the three O atoms are set to be equal.

Table 4 Selected bond parameters of deuterated jarosite

T (K)	K-O2(Å)	K-O3(Å)	S-O1(Å)	S-O2(Å)	Fe-O2(Å) ^a	Fe-O3(Å) ^b	D-O3(Å)	D...O1(Å)	Fe-O3-Fe(°)
298	2.9721(8)	2.823(1)	1.437(3)	1.479(1)	2.0501(9)	1.9815(4)	0.967(1)	1.952(1)	133.77(6)
350	2.9751(8)	2.828(1)	1.442(3)	1.477(1)	2.0493(9)	1.9825(4)	0.964(1)	1.961(1)	133.69(6)
375	2.9786(8)	2.832(1)	1.447(3)	1.474(1)	2.0501(9)	1.9831(4)	0.962(1)	1.966(1)	133.67(6)
400	2.9805(8)	2.834(1)	1.450(3)	1.472(1)	2.0499(9)	1.9841(4)	0.961(1)	1.970(1)	133.58(6)
425	2.9830(9)	2.836(1)	1.454(4)	1.471(1)	2.0500(9)	1.9847(5)	0.960(1)	1.974(1)	133.55(6)
450	2.9843(9)	2.839(1)	1.459(4)	1.469(2)	2.050(1)	1.9849(5)	0.958(1)	1.979(1)	133.55(6)
475	2.9852(9)	2.842(1)	1.459(4)	1.468(2)	2.051(1)	1.9853(5)	0.957(1)	1.983(2)	133.51(7)
500	2.9860(9)	2.843(1)	1.464(4)	1.465(2)	2.053(1)	1.9863(5)	0.954(1)	1.988(2)	133.40(7)
525	2.986(1)	2.844(1)	1.469(4)	1.463(2)	2.055(1)	1.9873(5)	0.951(1)	1.993(2)	133.40(7)
550	2.986(1)	2.845(1)	1.471(5)	1.460(2)	2.059(1)	1.9866(6)	0.946(1)	2.001(2)	133.38(8)
575	2.987(1)	2.846(2)	1.474(6)	1.458(2)	2.060(2)	1.9866(8)	0.946(2)	2.003(2)	133.37(10)

^aAverage of two Fe-O2 edges; ^bAverage of four Fe-O3 edges.

Figure Captions

- Fig. 1 (A) Crystal structure of jarosite, $\text{KFe}_3(\text{SO}_4)_2(\text{OH})_6$; (B) A sheet of $[\text{Fe}(\text{O},\text{OH})_6]$ octahedra and $[\text{SO}_4]$ tetrahedra projected along the c -axis; (C) Ball-and-stick representation of the jarosite structure. Tetrahedra represent $[\text{SO}_4]$ units, octahedra represent $[\text{Fe}(\text{O},\text{OH})_6]$ units, pink balls represent K, green balls represent Fe, brown balls represent S, blue balls represent O (light blue – O1 and O2; dark blue – O3), and red balls represent H. Blue lines in A and B outline the unit cell, and the dash line in C marks the hydrogen bond between O1 and H. In A and C, the c -axis of the jarosite structure is vertical.
- Fig. 2 A pair of fitted neutron diffraction patterns of deuterated jarosite collected at (A) $2\theta = 90^\circ$ and (B) $2\theta = 140^\circ$ at 298 K. Data are shown as plus signs, and the solid curve is the best fit to the data. Tick marks below the pattern show the positions of allowed reflections, and the lower curve represents the difference between the observed and calculated profiles.
- Fig. 3 Neutron diffraction patterns ($2\theta = 90^\circ$) of the deuterated jarosite sample collected at 550K, 575 K, 600 K, and 625 K. At 575 K, jarosite started to decompose into yavapaiite and hematite, as evidenced by the appearance of their diffraction peaks (e.g., hematite 104 and yavapaiite 111/-201). The decomposition was completed at 625 K, as indicated by the disappearance of jarosite peaks such as 003.
- Fig. 4 Variation of unit-cell parameters (A) a , (B) c , and (C) cell volume V of deuterated jarosite with temperature.

Fig. 5 Variation of isotropic atomic displacement parameters (U_{iso}) of K, S, Fe, O and D in deuterated jarosite with temperature.

Fig. 6 Variation of interatomic distances (A) D \cdots O1 and (B) O3-D in deuterated jarosite as a function of temperature.

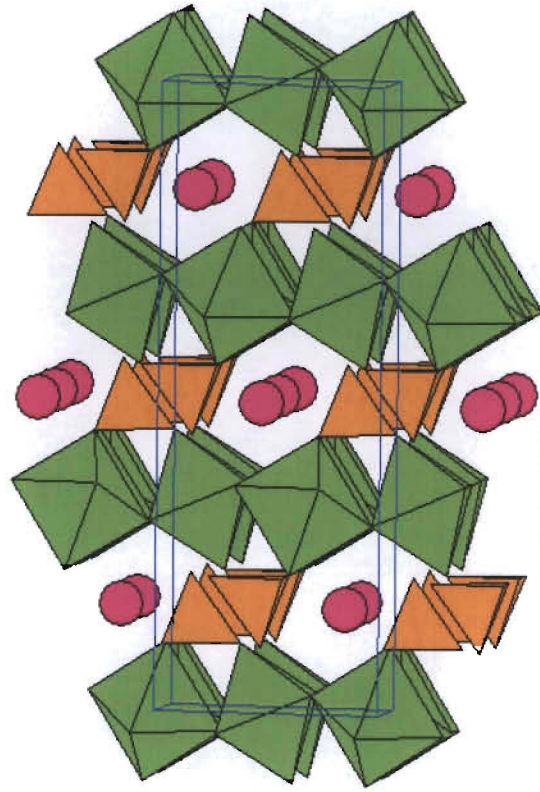


Fig. 1A

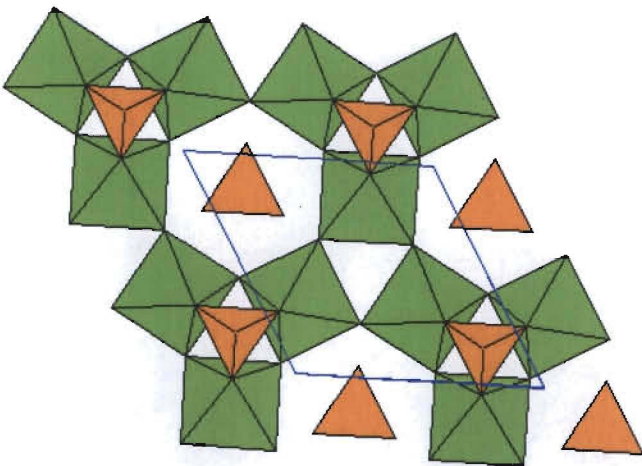


Fig. 1B

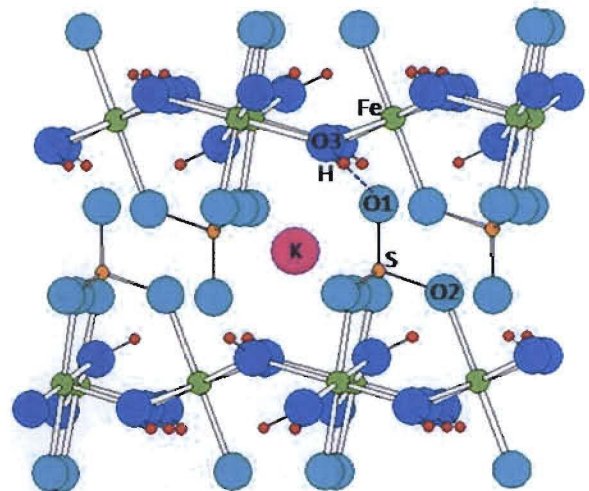


Fig. 1C

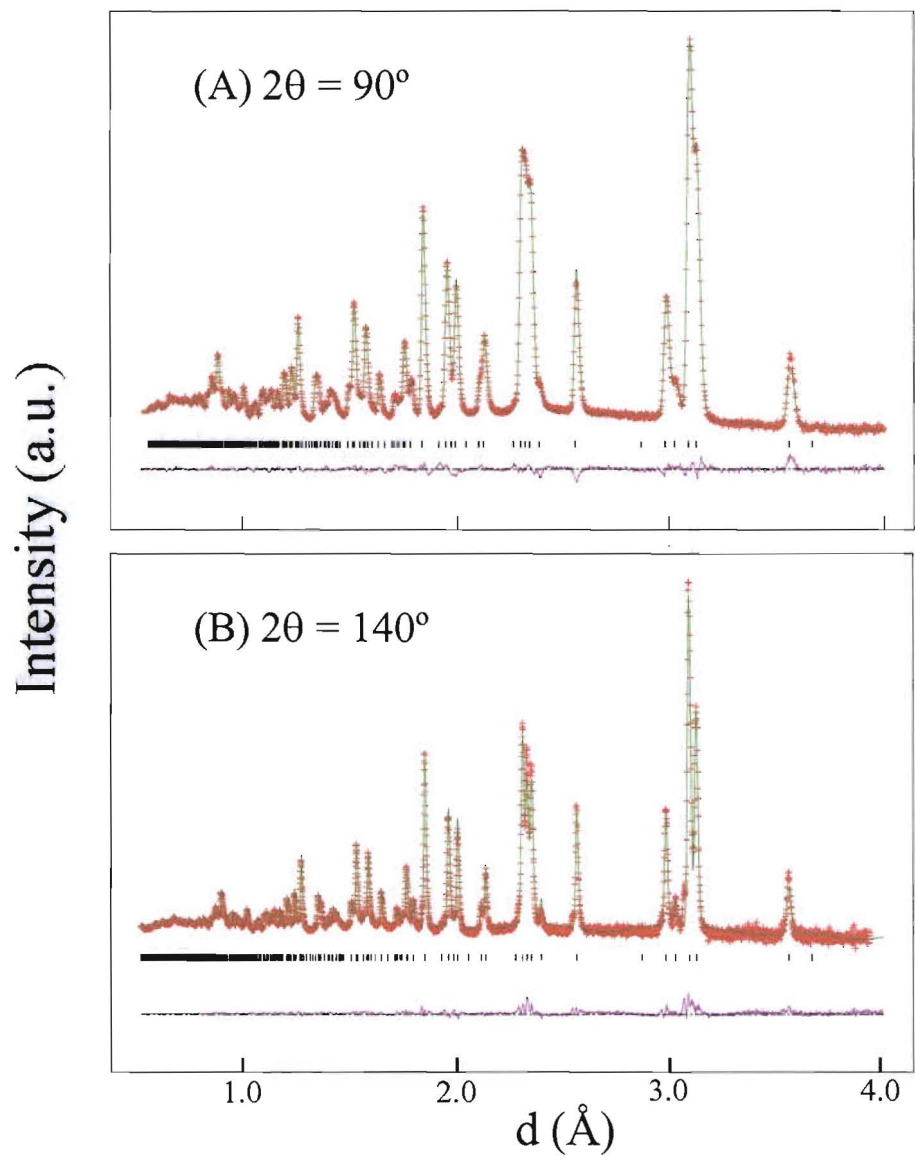


Fig. 2

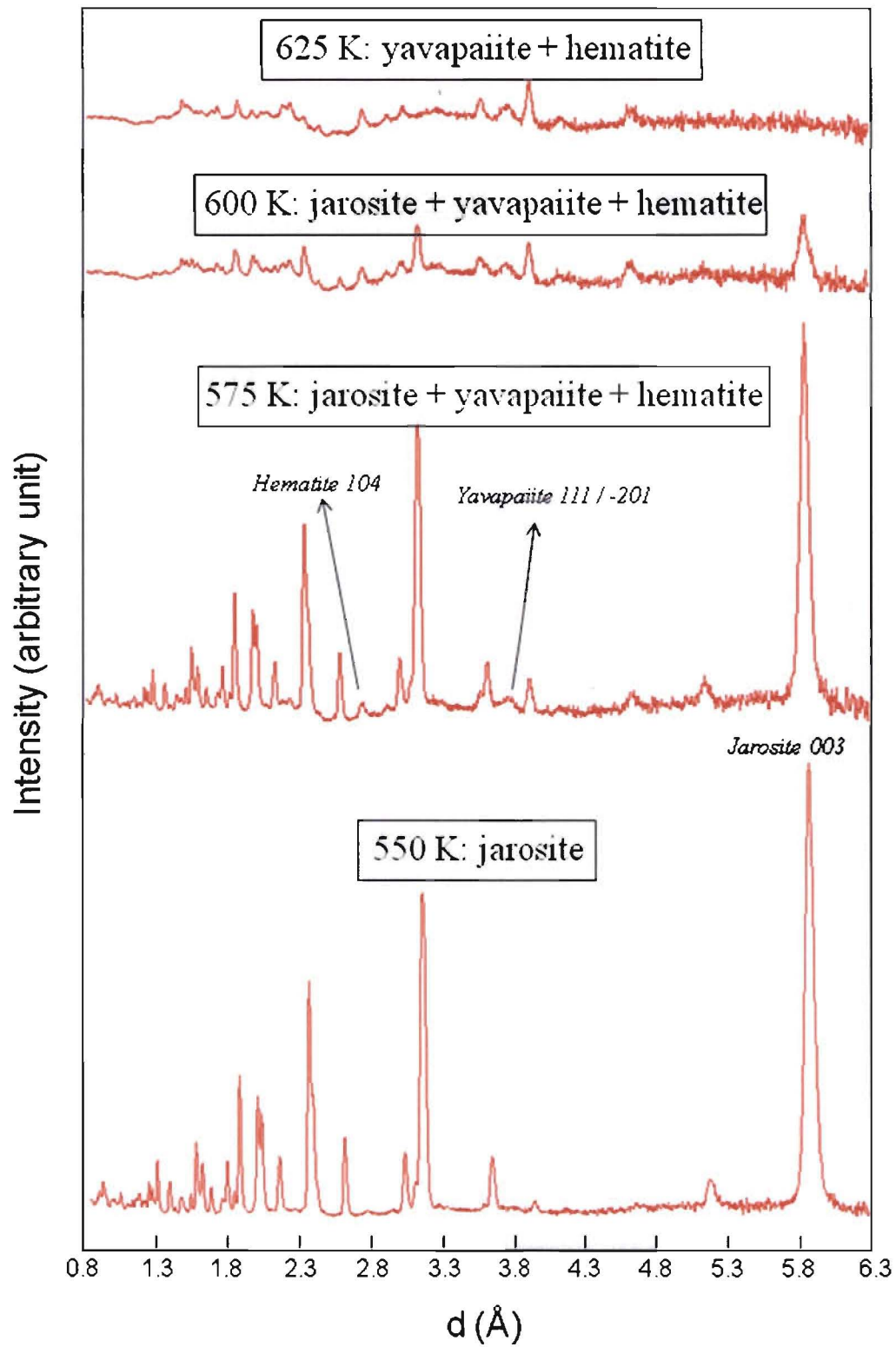


Fig. 3

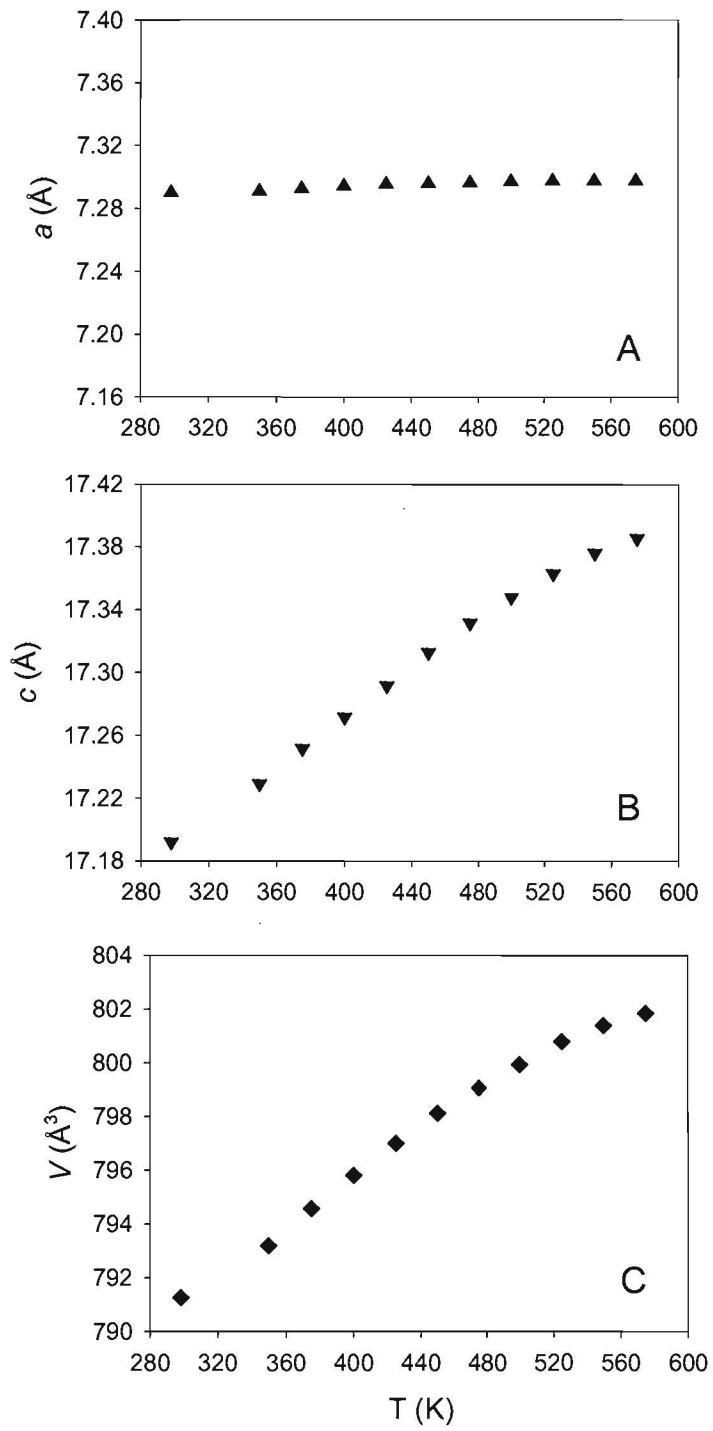


Fig. 4

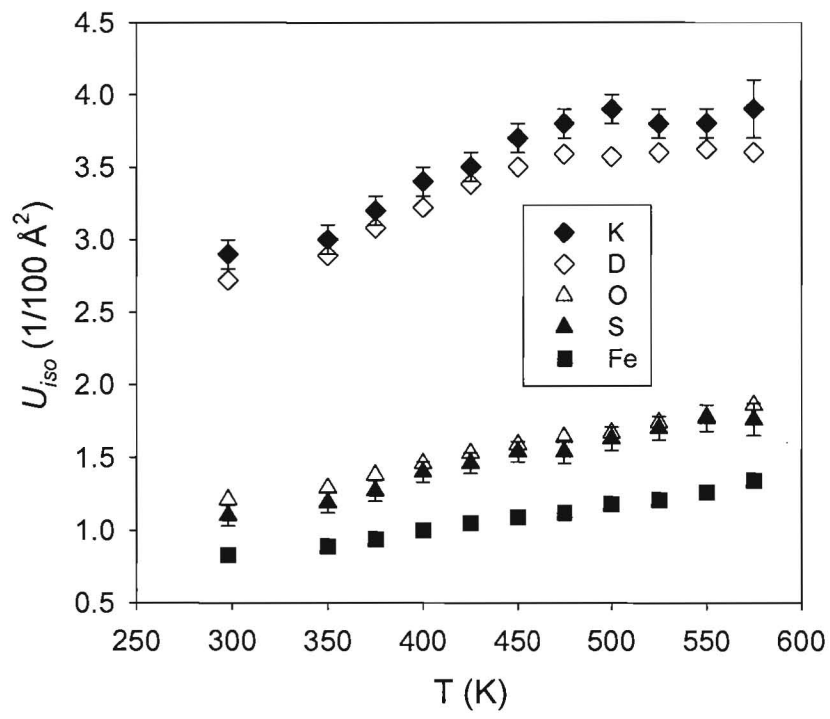


Fig. 5

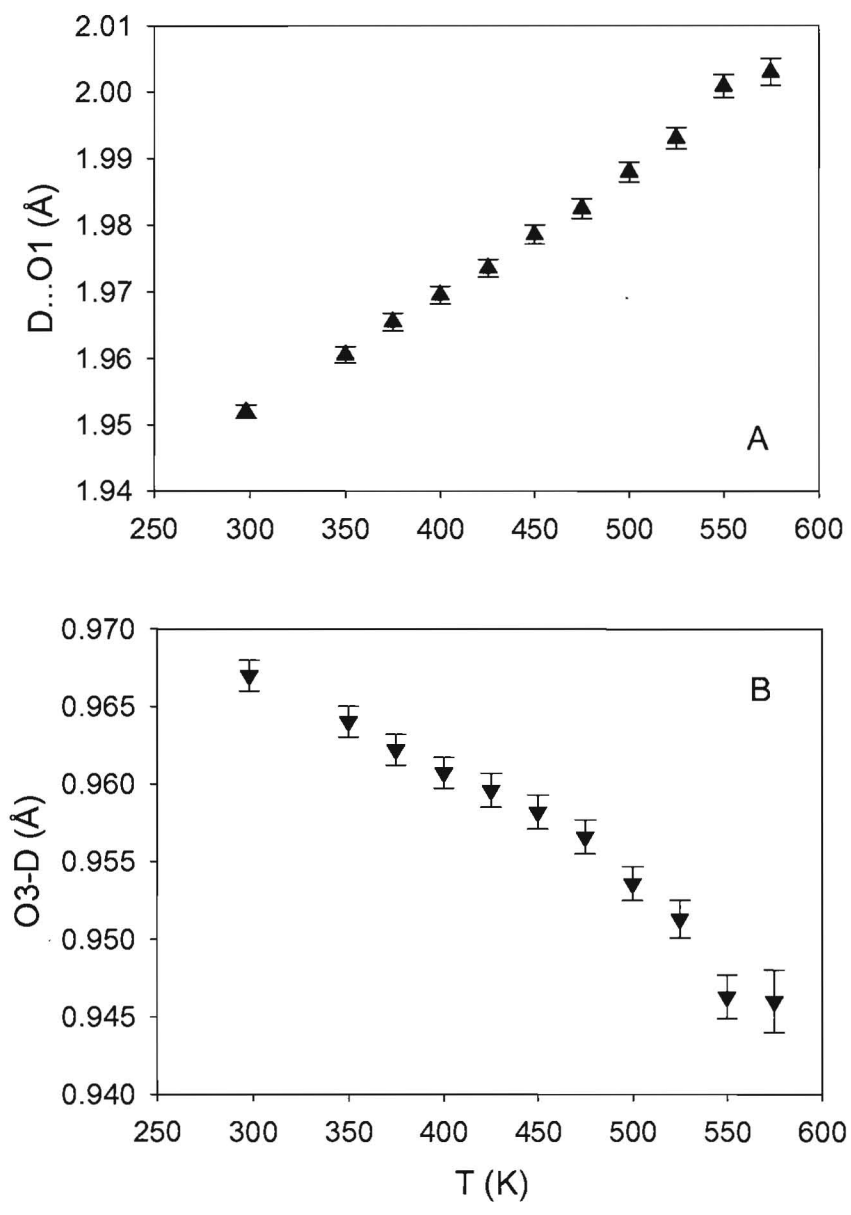


Fig. 6